

Octupole correlations in light actinides from the interacting boson model based on the Gogny energy density functional

Nomura, Kosuke; Rodríguez-Guzmán, R.; Humadi, Y. M.; Robledo, L. M.; García-Ramos, J. E.

Source / Izvornik: **Physical Review C (nuclear physics), 2020, 102**

Journal article, Published version

Rad u časopisu, Objavljena verzija rada (izdavačev PDF)

<https://doi.org/10.1103/PhysRevC.102.064326>

Permanent link / Trajna poveznica: <https://um.nsk.hr/um:nbn:hr:217:836999>

Rights / Prava: [In copyright](#)/[Zaštićeno autorskim pravom.](#)

Download date / Datum preuzimanja: **2024-09-12**






Repository / Repozitorij:

[Repository of the Faculty of Science - University of Zagreb](#)



Octupole correlations in light actinides from the interacting boson model based on the Gogny energy density functional

K. Nomura ^{1,*}, R. Rodríguez-Guzmán,² Y. M. Humadi ², L. M. Robledo ^{3,4} and J. E. García-Ramos ^{5,6}

¹*Department of Physics, Faculty of Science, University of Zagreb, HR-10000 Zagreb, Croatia*

²*Physics Department, Kuwait University, 13060 Kuwait, Kuwait*

³*Departamento de Física Teórica and CIAFF, Universidad Autónoma de Madrid, E-28049 Madrid, Spain*

⁴*Center for Computational Simulation, Universidad Politécnica de Madrid, Campus de Montegancedo, Bohadilla del Monte, E-28660-Madrid, Spain*

⁵*Departamento de Ciencias Integradas y Centro de Estudios Avanzados en Física, Matemática y Computación, Universidad de Huelva, E-21071 Huelva, Spain*

⁶*Instituto Carlos I de Física Teórica y Computacional, Universidad de Granada, Fuentenueva s/n, 18071 Granada, Spain*



(Received 20 August 2020; accepted 7 December 2020; published 28 December 2020)

The quadrupole-octupole coupling and the related spectroscopic properties have been studied for the even-even light actinides $^{218-238}\text{Ra}$ and $^{220-240}\text{Th}$. The Hartree-Fock-Bogoliubov approximation, based on the Gogny-DIM energy density functional, has been employed as a microscopic input, i.e., to obtain (axially symmetric) mean-field potential energy surfaces as functions of the quadrupole and octupole deformation parameters. The mean-field potential energy surfaces have been mapped onto the corresponding bosonic potential energy surfaces using the expectation value of the *sdf* interacting boson model (IBM) Hamiltonian in the boson condensate state. The strength parameters of the *sdf* IBM Hamiltonian have been determined via this mapping procedure. The diagonalization of the mapped IBM Hamiltonian provides energies for positive- and negative-parity states as well as wave functions which are employed to obtain transitional strengths. The results of the calculations compare well with available data from Coulomb excitation experiments and point towards a pronounced octupole collectivity around ^{224}Ra and ^{226}Th .

DOI: [10.1103/PhysRevC.102.064326](https://doi.org/10.1103/PhysRevC.102.064326)

I. INTRODUCTION

It is a well-known fact that just a handful of nuclei exhibit reflection-asymmetric ground states with nonzero octupole deformation. Reflection-asymmetric shapes are favored in some very specific regions of the nuclear chart with neutron N and/or proton Z numbers around 34, 56, 88, 136, . . . [1,2]. However, dynamical octupole correlations have attracted considerable attention in recent years as they play a relevant role in the description of many negative-parity collective states like the low-lying 1^- states in the spectra of even-even nuclei that are usually considered fingerprints of octupole correlations [3,4]. In the common situation where the ground state of those nuclei is quadrupole deformed, there exists a 3^- state member of the corresponding negative-parity rotational band, which decays through fast $E3$ transitions to the 0^+ ground state. However, the decay of the 1^- to the ground state proceeds via $E1$ transitions. The study of these as well as other features associated with octupole correlations, like the existence of alternating-parity rotational bands, has become an active research field with several experiments planned or already operational at state-of-the-art radioactive-ion beam facilities around the world. Within this context, evidence of octupolarity has been found in the case of the light actinides (^{220}Rn ,

^{224}Ra , and $^{222,228}\text{Ra}$ [5,6]) and lanthanides ($^{144,146}\text{Ba}$ [7,8]). The study of octupole correlations also has a potential impact on other research fields. Indeed, the presence of static (and dynamic) nuclear octupole correlations enhances the fingerprints of the existence of a nonzero electric dipole moment of elementary particles. The existence of such an effect would imply the violation of the CP symmetry, implying the existence of new physics beyond the standard model of particle physics [9].

From a theoretical point of view, both relativistic [10,11] and nonrelativistic [12,13] approaches rooted in the nuclear energy density functional (EDF) framework [12] have been extensively employed to describe intrinsic nuclear shapes and the related spectroscopic properties. In particular, the static and dynamic aspects associated with the spontaneous breaking of reflection symmetry have been studied using the self-consistent mean-field (SCMF) approximation based on a given nonrelativistic or relativistic EDF [3,4,14–39]. Dynamical beyond-mean-field correlations, stemming from symmetry restoration and/or fluctuations in the relevant collective deformations, have been considered within configuration mixing approaches in the spirit of the generator coordinate method (GCM) [12,13,40].

On the one hand, beyond-mean-field configuration-mixing approaches are required to access spectroscopic properties such as the excitation energies of negative-parity states as well

*knomura@phy.hr

as $B(E1)$ and $B(E3)$ reduced transition probabilities. On the other hand, beyond-mean-field approaches become computationally expensive in medium and heavy nuclei, especially when several collective coordinates are to be included in the GCM ansatz. This drawback of the GCM justifies the introduction of computationally less expensive approaches like the interacting boson model (IBM) mapping procedures introduced in Refs. [41,42]. In this approach, the SCMF potential energy surfaces (PESs) are mapped onto the corresponding (bosonic) IBM PESs as to determine some of the strength parameters of the corresponding IBM Hamiltonian, which is subsequently used to compute excitation spectra and transition probabilities. The method has been employed to study octupole-related effects like the surveys of octupole-related properties in the rare-earth and actinide regions [43–45] or the description of octupole bands in neutron-rich odd-mass nuclei [46]. The SCMF PESs have been computed using the relativistic density-dependent point coupling (DD-PC1) [47] or the nonrelativistic Gogny-D1M [48,49] EDFs.

Due to the renewed experimental interest in the light actinide region, we consider in this work the evolution of the octupole shapes and the resulting spectroscopic properties in a wide range of actinide nuclei including $^{218-238}\text{Ra}$ and $^{220-240}\text{Th}$. To this end, the quadrupole-octupole SCMF PESs, obtained within the (axially symmetric) Hartree-Fock-Bogoliubov (HFB) approximation based on the parametrization D1M [49] of the Gogny EDF [48], are mapped onto the expectation value of the interacting-boson Hamiltonian in the condensate state consisting of the monopole $L = 0^+$ (s), quadrupole 2^+ (d), and octupole 3^- (f) bosons [50,51]. The mapping procedure, employed to obtain the IBM PESs from the SCMF PESs, completely determines the considered quadrupole-octupole sd f IBM Hamiltonian and its diagonalization provides wave functions which are subsequently used to compute positive- and negative-parity spectra as well as transition strengths. Furthermore, by comparing with our previous spectroscopic calculations based on the relativistic EDF DD-PC1 [43,44], we demonstrate the robustness of the SCMF-to-IBM mapping procedure. At a qualitative (and often quantitative) level the main results and conclusions obtained in the paper remain the same regardless of whether a relativistic or nonrelativistic energy density functional is taken as the microscopic input. Likely, this is a consequence of both DD-PC1 and D1M being fitted to binding energies of finite nuclei. In addition, the present analysis not only covers those nuclei considered in Refs. [43,44], but also explores even heavier isotopes toward the neutron number $N = 150$, in which experimental information is not yet available. In the present study we also discuss some quantities not covered in Refs. [43,44].

The paper is organized as follows. The Gogny-D1M quadrupole-octupole SCMF PESs, i.e., the microscopic building blocks of the calculations, are discussed in Sec. II. The mapping procedure to obtain the IBM Hamiltonian is illustrated in Sec. III. The results obtained for low-energy excitation spectra, electric quadrupole, octupole and dipole transition strengths, as well as for the transition quadrupole and octupole moments are discussed in Sec. IV. Finally, Sec. V is devoted to the concluding remarks and work perspectives.

II. SCMF GOGNY-D1M CALCULATIONS

To obtain the quadrupole-octupole SCMF PESs, the HFB equation has been solved with constraints on the axially symmetric quadrupole \hat{Q}_{20} and octupole \hat{Q}_{30} operators [29,45]:

$$\begin{aligned}\hat{Q}_{20} &= z^2 - \frac{1}{2}(x^2 + y^2), \\ \hat{Q}_{30} &= z^3 - \frac{3}{2}z(x^2 + y^2).\end{aligned}\quad (1)$$

The mean values $\langle \Phi_{\text{HFB}} | \hat{Q}_{20} | \Phi_{\text{HFB}} \rangle = Q_{20}$ and $\langle \Phi_{\text{HFB}} | \hat{Q}_{30} | \Phi_{\text{HFB}} \rangle = Q_{30}$ also define the quadrupole and octupole deformation parameters β_{20} and β_{30} :

$$\beta_{\lambda 0} = \frac{\sqrt{4\pi(2\lambda + 1)}}{3R_0^\lambda A} Q_{\lambda 0}, \quad (2)$$

where $R_0 = 1.2A^{1/3}$ fm. In the following, the subscript zero in $\beta_{\lambda 0}$'s and $Q_{\lambda 0}$'s ($\lambda = 2, 3$) is omitted, unless otherwise specified. The center of mass is fixed at the origin to avoid spurious effects associated with its motion [29,30]. The HFB quasiparticle operators [40] have been expanded in a deformed (axially symmetric) harmonic oscillator (HO) basis containing 17 major shells to grant convergence for the studied physical quantities.

The constrained calculations provide a set of HFB states $|\Phi_{\text{HFB}}(\beta_2, \beta_3)\rangle$ labeled by their static deformation parameters β_2 and β_3 . The HFB energies $E_{\text{HFB}}(\beta_2, \beta_3)$ associated with those HFB states define the contour plots referred to as SCMF PESs in this work. As the HFB energies satisfy the property $E_{\text{HFB}}(\beta_2, \beta_3) = E_{\text{HFB}}(\beta_2, -\beta_3)$, only positive β_3 values are considered when plotting the SCMF PESs.

The SCMF PESs obtained for $^{218-238}\text{Ra}$ and $^{220-240}\text{Th}$ are depicted in Fig. 1. Along the β_2 direction there is a shape and/or phase transition from spherical or weakly deformed ground states in the lightest isotopes (^{218}Ra and ^{220}Th) to well quadrupole deformed ground states in heavier nuclei. On the other hand, the SCMF PESs are rather soft along the β_3 direction. A global octupole deformed minimum with $\beta_3 \approx 0.1$ already emerges for $N \approx 132$ (^{220}Ra and ^{222}Th). This minimum becomes deeper as one approaches the neutron number $N = 136$ (^{224}Ra and ^{226}Th). In our calculations the most pronounced octupole deformation effects are found around this neutron number with $\beta_3 \approx 0.15$ for ^{224}Ra and ^{226}Th , in good agreement with the experiment [1]. Beyond this neutron number, as one moves towards $N = 150$, the corresponding β_3 values decrease and reflection-symmetric HFB ground states are obtained for the heaviest isotopes in both chains.

Previous SCMF calculations including the quadrupole and octupole constraints simultaneously can be found in the literature for nuclei in this region of the nuclear chart. For example, calculations were carried out in Ref. [44] for $^{218-228}\text{Ra}$ and $^{220-232}\text{Th}$ using the relativistic DD-PC1 EDF [47]. The overall systematics of the quadrupole and octupole deformations associated with the DD-PC1 SCMF PESs is similar to that obtained in the present study with the Gogny-D1M EDF. However, in the case of the DD-PC1 EDF, the $N = 132$ isotopes (^{220}Ra and ^{222}Th) exhibit a reflection-symmetric SCMF ground state while those nuclei are predicted to be octupole

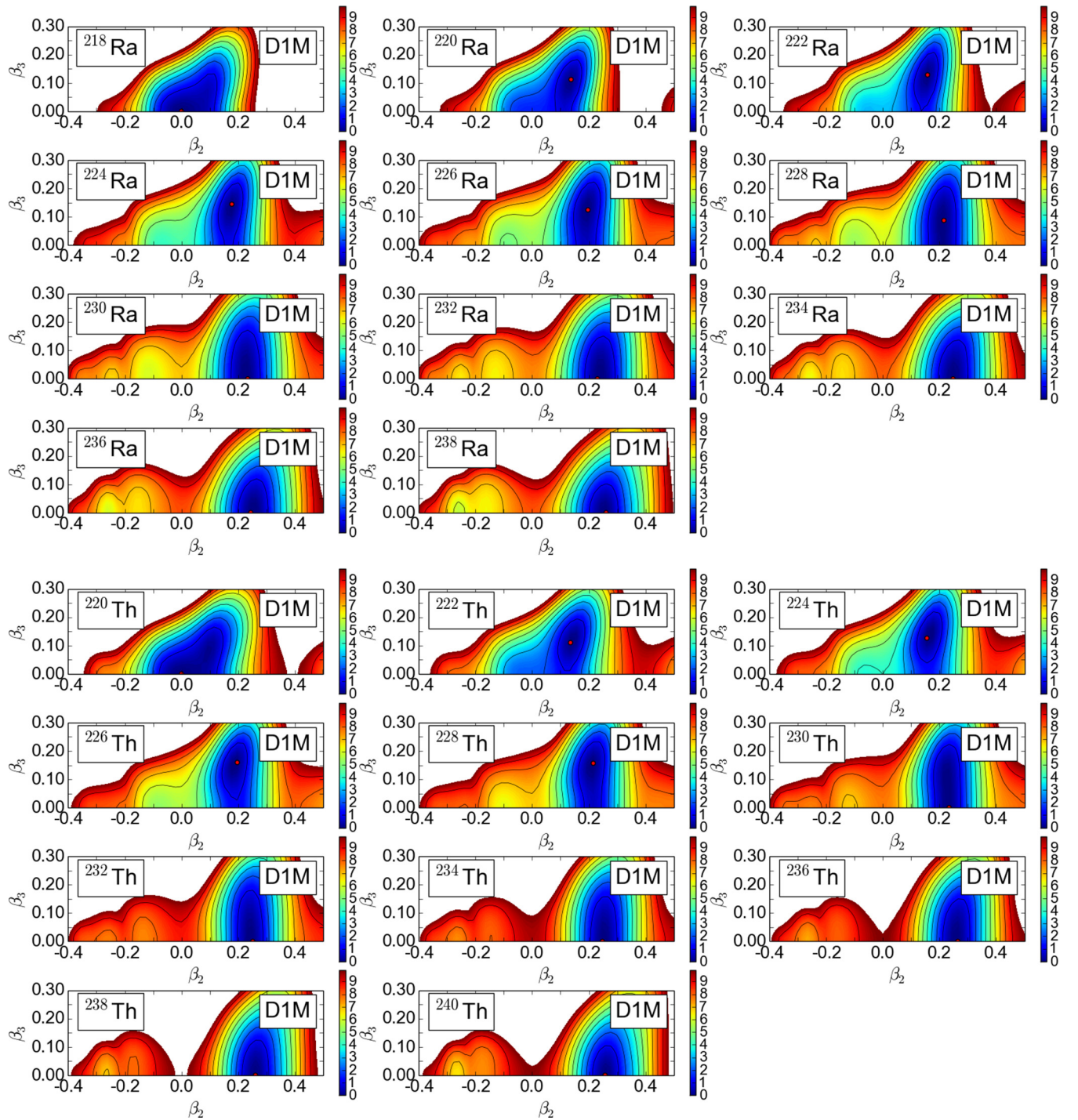


FIG. 1. SCMF-PESs computed with the Gogny-D1M EDF for the nuclei $^{218-238}\text{Ra}$ and $^{220-240}\text{Th}$. The color code indicates the total HFB energies in MeV units, plotted up to 10 MeV with respect to the global minimum. For each nucleus, the global minimum is indicated by a solid circle. For more details, see the main text.

deformed in the Gogny-D1M calculations. Pronounced octupole deformation effects are predicted by both EDFs for ^{224}Ra and ^{226}Th though deeper global minima are found in the relativistic approach. The quadrupole-octupole coupling was studied for Rn, Ra, and Th nuclei in Ref. [30]. A comparison of several relativistic EDFs in a survey of octupole correlations can be found in Ref. [32]. A thorough account

over a large set of even-even nuclei of observables associated to octupole correlations was presented in Refs. [3,4] using the Gogny-HFB approach, parity projection, and octupole configuration mixing. Octupole deformations have also been studied for Ra isotopes [26] using the HFB approach based on the Barcelona-Catania-Paris (BCP) [26] and Gogny-D1S [52] EDFs.

III. MAPPING ONTO THE BOSON SYSTEM

Having the (fermionic) Gogny-D1M SCMF PESs at hand, we map them onto the corresponding (bosonic) IBM PESs using the methods developed in Refs. [41–43]. To account for negative-parity states, the IBM space includes, in addition to the positive-parity monopole s ($L = 0^+$) and quadrupole d ($L = 2^+$) bosons, the negative-parity f ($L = 3^-$) boson. Within the IBM framework, bosons represent collective pairs of valence nucleons [53]. In particular, the f boson can be viewed as formed by coupling the normal and unique parity orbitals $\pi(i_{13/2} \otimes f_{7/2})^{(3^-)}$ and $\nu(j_{15/2} \otimes g_{9/2})^{(3^-)}$ in the light actinides with $Z \approx 88$ and $N \approx 136$. In the usual sdf -IBM phenomenology, the number of f bosons involved in the IBM space is limited to one or, at most, three. In the present work, we do not assume any such truncation for the f -boson number. Thus, the numbers n_s , n_d , and n_f of s , d , and f bosons are arbitrary and satisfy the condition that the total boson number $N_B = n_s + n_d + n_f$ is conserved for a given nucleus.

The mapping of the Gogny-D1M (β_2, β_3) PESs onto the IBM ones is achieved by introducing the intrinsic state for the boson system [54]:

$$|\phi\rangle = \frac{1}{\sqrt{N_B!}} (b_c^\dagger)^{N_B} |0\rangle, \quad (3)$$

where N_B and $|0\rangle$ denote the number of bosons and the boson vacuum, respectively. The condensate boson operator b_c^\dagger is given by

$$b_c^\dagger = (1 + \alpha_2^2 + \alpha_3^2)^{-1/2} (s^\dagger + \alpha_2 d_0^\dagger + \alpha_3 f_0^\dagger), \quad (4)$$

with amplitudes α_2 and α_3 . The doubly-magic nucleus ^{208}Pb is taken as a boson vacuum. Therefore, N_B runs from 5 to 15 (6 to 16) for $^{218-238}\text{Ra}$ ($^{220-240}\text{Th}$). The amplitudes α_2 and α_3 can be related to the deformation parameters β_2 and β_3 as $\alpha_2 = C_2\beta_2$ and $\alpha_3 = C_3\beta_3$ [44,45,54], where C_2 and C_3 represent dimensionless parameters.

The IBM PES is obtained analytically, by taking the expectation value of the sdf -IBM Hamiltonian in the boson condensate state [Eq. (3)]. The sdf -IBM Hamiltonian is the sum of the Hamiltonians for the sd and f boson spaces plus a coupling \hat{H}_{sdf} between them:

$$\hat{H} = \hat{H}_{sd} + \hat{H}_f + \hat{H}_{sdf}. \quad (5)$$

The sd -boson Hamiltonian reads

$$\hat{H}_{sd} = \epsilon_d \hat{n}_d + \kappa_{sd} \hat{Q}_{sd} \cdot \hat{Q}_{sd} + \kappa'_{sd} \hat{L}_d \cdot \hat{L}_d, \quad (6)$$

where the first term represents the number operator for the d bosons with ϵ_d being the single d -boson energy relative to the s -boson one. The second term represents the quadrupole-quadrupole interaction with strength κ_{sd} and the quadrupole operator $\hat{Q}_{sd} = s^\dagger \tilde{d} + d^\dagger \tilde{s} + \chi_{dd} [d^\dagger \times \tilde{d}]^{(2)}$. The third term in Eq. (6) is the rotational term with the angular momentum operator $\hat{L}_d = \sqrt{10} [d^\dagger \times \tilde{d}]^{(1)}$.

The Hamiltonian for the f -boson space reads

$$\hat{H}_f = \epsilon_f \hat{n}_f + \kappa_f \hat{Q}_f \cdot \hat{Q}_f + \kappa'_f \hat{L}_f \cdot \hat{L}_f, \quad (7)$$

with the f -boson quadrupole operator \hat{Q}_f and angular momentum operator \hat{L}_f being $\hat{Q}_f = [f^\dagger \times \tilde{f}]^{(2)}$ and $\hat{L}_f = \sqrt{28} [f^\dagger \times \tilde{f}]^{(1)}$, respectively.

The sdf Hamiltonian employed here takes the following form:

$$\hat{H}_{sdf} = \kappa'_{sdf} \hat{Q}_{sd} \cdot \hat{Q}_f + \kappa_{sdf} \hat{O} \cdot \hat{O}. \quad (8)$$

The last term in Eq. (8) is the octupole-octupole interaction with the strength parameter κ_{sdf} . The octupole operator takes the form

$$\hat{O} = s^\dagger \tilde{f} + f^\dagger \tilde{s} + \chi_{df} [d^\dagger \times \tilde{f} + f^\dagger \times \tilde{d}]^{(3)}, \quad (9)$$

with χ_{df} being a parameter.

For convenience, we introduce a new parameter χ_{ff} so that $\kappa'_{sdf} = 2\kappa_{sd}\chi_{ff}$, and $\kappa_f = \kappa_{sd}\chi_{ff}^2$, and we assume $\kappa'_f = \kappa'_{sd}$. The independent parameters of the Hamiltonian are, therefore, ϵ_d , ϵ_f , κ_{sd} , κ'_{sd} , χ_{dd} , χ_{ff} , κ_{sdf} , and χ_{df} as well as the coefficients C_2 and C_3 for the β_2 and β_3 deformations. These parameters are determined via the mapping procedure. The Hamiltonian in Eq. (5) is similar to the one employed in our previous study in the rare-earth region [45], except for the $\hat{L}_f \cdot \hat{L}_f$ term considered in this work. This rotational correction term is considered because a good amount of f -boson components is present in the calculated yrast states for both parities and the inclusion of this term has a sizable effect on the moments of inertia obtained for the positive- and negative-parity yrast bands. A more detailed account of the other terms as well as the analytical form of the IBM PES as a function of the β_2 and β_3 deformations can be found in Ref. [45].

The strength parameters of the sdf -IBM Hamiltonian in Eq. (5) are determined so that the IBM PES reproduces the topology of the Gogny-D1M SCMF PES around the global minimum. Since the Hamiltonian (5) contains a large number of parameters, an unconstrained fitting can land in local minima far away from the physical solution. Therefore, it is always convenient to fit the parameters in a controlled, physically inspired way by using the following procedure: First, the strength parameters of the sd -boson space Hamiltonian \hat{H}_{sd} [Eq. (6)] (ϵ_d , κ_{sd} , χ_{dd} , and C_2) are fixed by carrying out the mapping along the $\beta_3 = 0$ axis in such a way that the curvature in β_2 around the absolute (prolate) minimum, the depth of the potential well, and the energy difference between the prolate and oblate minima are reproduced. Only the parameter κ'_{sd} for the $\hat{L}_d \cdot \hat{L}_d$ term in Eq. (6) is determined independently in such a way that the bosonic cranking moment of inertia (see Ref. [55] for details) at the absolute minimum along the $\beta_3 = 0$ axis matches the Thouless-Valatin [56] moment of inertia for the 2^+ state computed with the reflection-symmetric SCMF cranking model. Second, the strength parameters related to the f -boson space Hamiltonian \hat{H}_f [Eq. (7)] and the ones related to the coupling between sd - and f -boson spaces \hat{H}_{sdf} [Eq. (8)] (ϵ_f , χ_{ff} , κ_{sdf} , χ_{df} , and C_3) are determined in such a way that the following features of the SCMF PES in the (β_2, β_3) space are reproduced as closely as possible: curvatures along the β_2 and β_3 directions around the global minimum, location of the minimum, and steepness of the potential both in β_2 and β_3 directions.

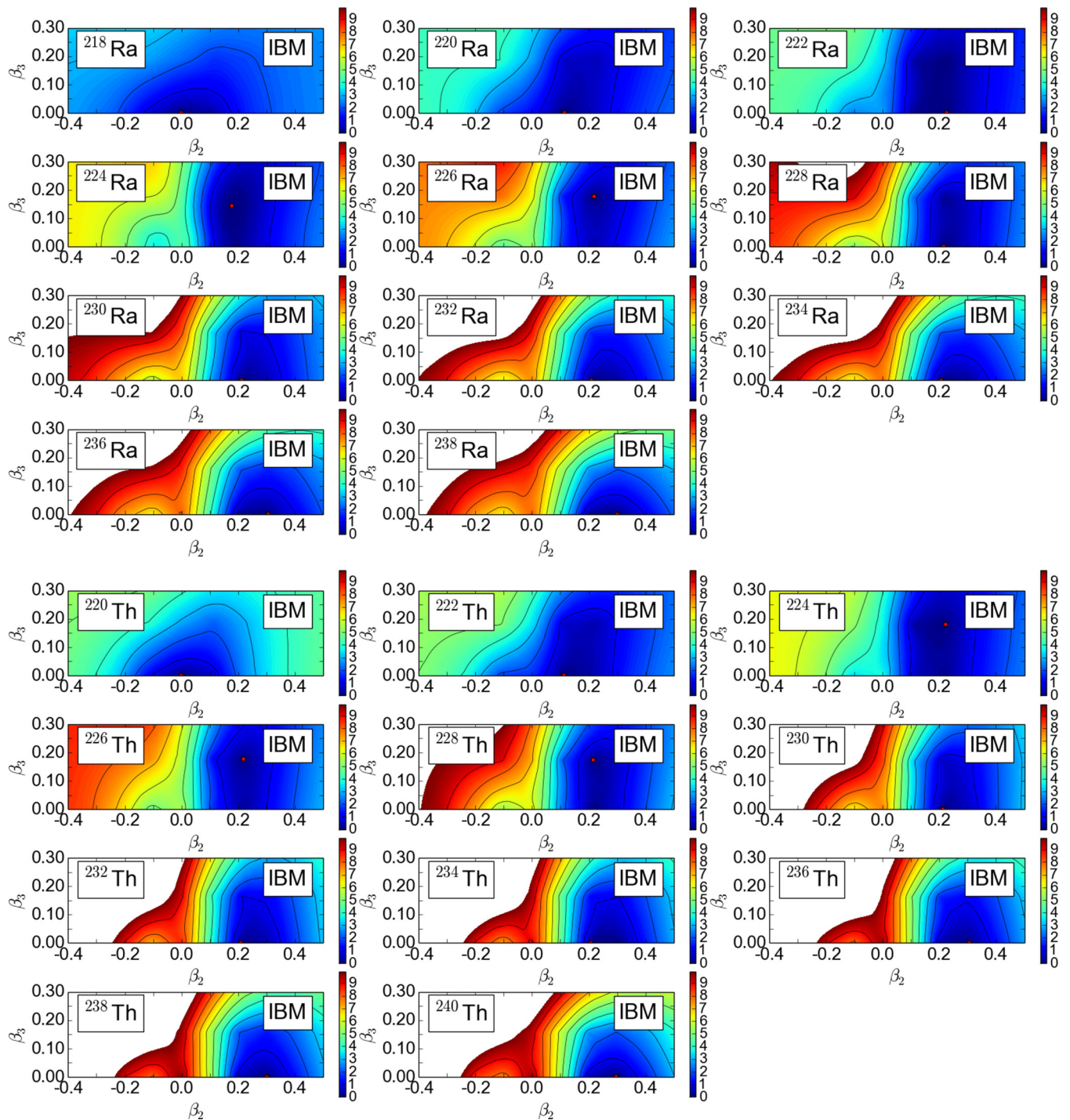


FIG. 2. IBM PESs computed with the mapped *sdf* IBM Hamiltonian [Eq. (5)] for the nuclei $^{218-238}\text{Ra}$ and $^{220-240}\text{Th}$. For more details, see the main text.

To uniquely determine the parameters, the following constraints are also considered, so as to be more or less consistent with our previous results [43–45] and earlier phenomenological studies within the *sdf*-IBM framework on the same mass region (e.g., Refs. [57,58]): (i) each parameter should evolve gradually with boson number; (ii) since most of the considered nuclei are strongly quadrupole deformed, the parameter χ_{dd} should take a value close to the one in the SU(3)

limit of the IBM, $\chi_{dd} = -1.32$ [50]; (iii) *d*-boson energy ϵ_d should decrease with boson number; (iv) ϵ_d should be lower in magnitude than the *f*-boson energy ϵ_f , except for the strongly octupole deformed nuclei around $N = 136$; and (v) the strengths κ_{sd} and κ_{sdf} should decrease in magnitude as the boson number increases.

The mapped *sdf*-IBM PESs are depicted in Fig. 2 for the studied nuclei. As expected, the original Gogny-D1M (β_2, β_3)

PESs are nicely reproduced around the global minimum. The IBM PESs are, however, much flatter far away from this minimum. This is a common feature found in previous IBM studies and can be attributed to the size of the IBM space [41,54]. The boson configuration space consists of only valence nucleons while all the nucleons are involved in the Gogny-HFB calculation. The resulting *sdf*-IBM Hamiltonian, with the strength parameters determined via the mapping procedure, is then diagonalized to obtain excitation energies and transition strengths for a given nucleus.

The strength parameters obtained for the *sdf*-IBM Hamiltonian are plotted in Figs. 3(a)–3(j) as functions of the neutron boson number N_ν , which equals $N_B - (Z - 82)/2$. The boson-number dependence of the parameters along an isotopic chain reflects the corresponding structural changes. Most of the parameters are smooth functions of N_ν . However, some of the parameters for the interaction terms involving *f* bosons, e.g., ϵ_f and χ_{df} , display abrupt changes around $N = 136$. This results from the difference in the topology of the SCMF PESs corresponding to neighboring isotopes in this transitional region (see Fig. 1).

IV. SPECTROSCOPIC PROPERTIES

A. Systematic of excitation spectra

The low-energy excitation spectra corresponding to even-spin positive- and odd-spin negative-parity yrast states are plotted in Fig. 4 as functions of the mass number A . Those states are assumed to be members of the $K^\pi = 0_1^+$ and 0_1^- bands. The excitation energies of the positive-parity states decrease with increasing neutron number. This reflects the onset of pronounced quadrupole deformation effects with increasing neutron number (see Figs. 1 and 2) and the corresponding transition from vibrational to well-developed rotational bands. For both isotopic chains, the predicted positive-parity spectra agree reasonably well with the experimental ones also included in the figure.

The excitation energies of the negative-parity states exhibit a parabolic behavior as functions of the neutron number. The lowest excitation energies correspond to $N \approx 136$ isotopes. Around this neutron number the predicted negative-parity band lies quite close in energy to the positive-parity band. This situation corresponds to an alternating-parity rotational band (see Sec. IV B) that is a neat fingerprint of permanent octupole deformation [1]. For larger neutron numbers, the negative-parity band is higher in energy and completely decoupled from the positive-parity band; i.e., the octupole vibrational regime, associated with the β_3 softness of the potential, sets in. The predicted excitation energies of the negative-parity states are also in good agreement with the experimental data though the former somewhat overestimates the latter, in particular around $N = 136$. In the case of the lightest isotopes ^{218}Ra and ^{220}Th , the predicted excitation energies for both parities are too high. This may be a consequence of the reduced IBM space employed in the calculations, which is not large enough to account for the low-lying structures of those nuclei close to the $N = 126$ neutron shell closure. Note also that for $^{218,220}\text{Ra}$ and $^{220,222}\text{Th}$ the 1^- energy level is predicted

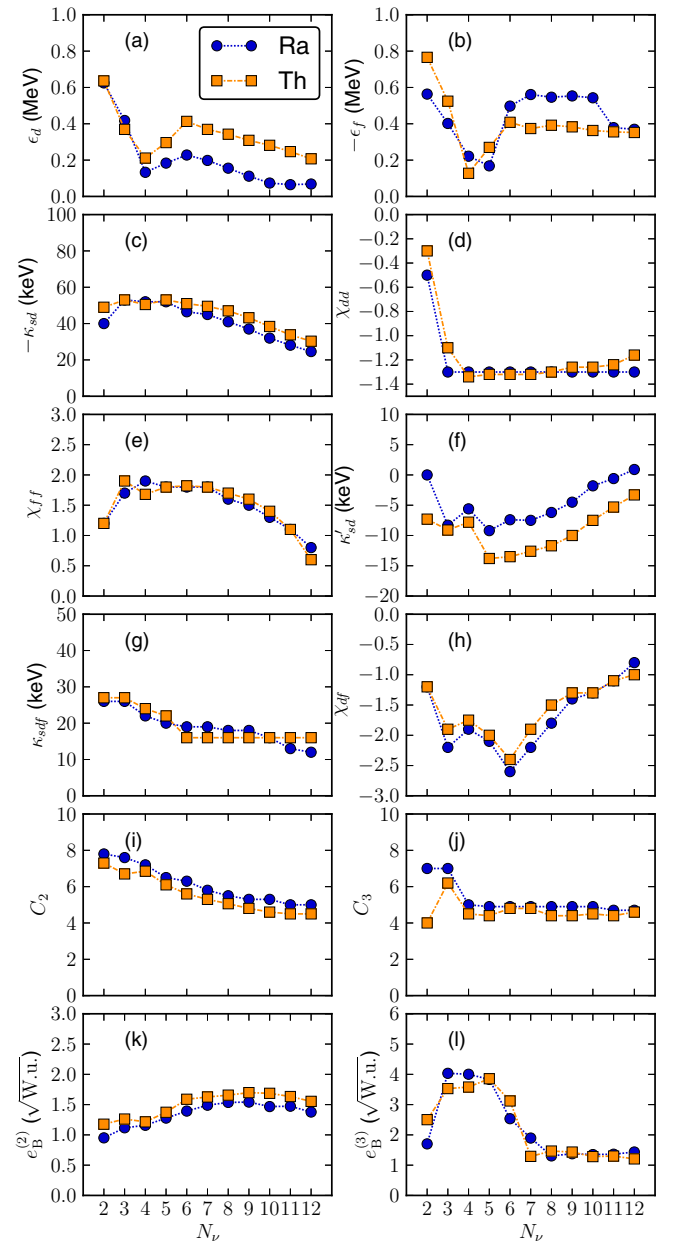


FIG. 3. The strength parameters of (a–h) the *sdf* IBM Hamiltonian [Eqs. (6)–(9)], (i, j) the coefficients C_λ for the deformation parameters, and (k, l) the boson effective charges $e_B^{(\lambda)}$ [Eqs. (14) and (15)] are plotted as functions of the neutron boson number N_ν for $^{218-238}\text{Ra}$ and $^{220-240}\text{Th}$.

above the 3^- level. In the case of ^{220}Ra this contradicts the experiment. This inversion could be, once more, the result of the limited IBM space employed in the calculations.

The present mapped *sdf*-IBM calculations, which are based on the Gogny-D1M EDF, are able to reproduce the observed positive- and negative-parity excitation spectra as nicely as our previous calculations [43,44] employing the relativistic DD-PC1 functional. The same is true for transition strength properties. This agreement confirms the robustness of the SCMF-to-IBM mapping procedure: results and

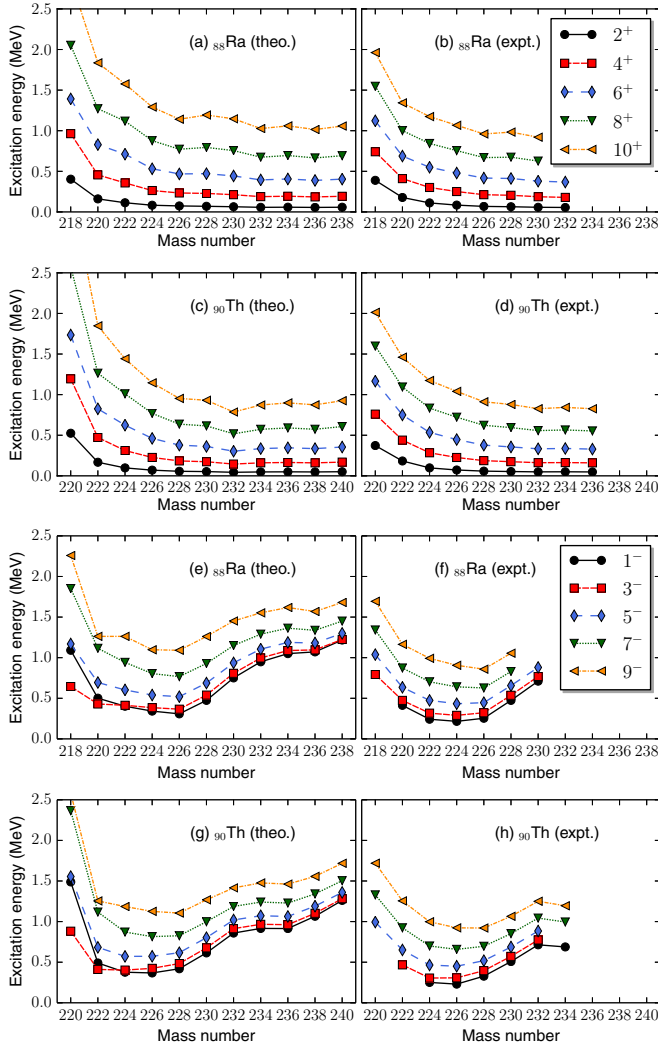


FIG. 4. Low-energy even-spin positive- and odd-spin negative-parity excitation spectra of yrast states for $^{218-238}\text{Ra}$ and $^{220-240}\text{Th}$ computed with the *sdf*-IBM Hamiltonian [Eq. (5)]. Experimental data are taken from Ref. [59].

conclusions do not differ at the qualitative (and most of the time, quantitative) level, regardless of whether a relativistic or nonrelativistic energy density functional is employed as the microscopic input.

The probability amplitudes of the *f*-boson components in the IBM wave functions corresponding to even-spin positive-parity and odd-spin negative-parity yrast states in $^{218-238}\text{Ra}$ and $^{220-240}\text{Th}$ are plotted in Fig. 5 as functions of the spin *I*. The amplitudes are computed as expectation values $\langle \hat{n}_f \rangle$ of the *f*-boson number operator \hat{n}_f [Eq. (7)] in the IBM wave functions. For all the studied isotopes, at low spins $I^\pi \leq 4^+$, the fraction of the *f* bosons in the positive-parity states is rather low. However, for spins $I^\pi \geq 6^+$ the contribution from the *f*-boson components increases in nuclei with neutron numbers $130 \leq N \leq 136$. A similar observation applies to negative-parity states. As can be seen from Figs. 5(c) and 5(d), the *f*-boson contributions become significant for $I^\pi > 7^-$. For both parities and isotopic chains, the *f* bosons play a major

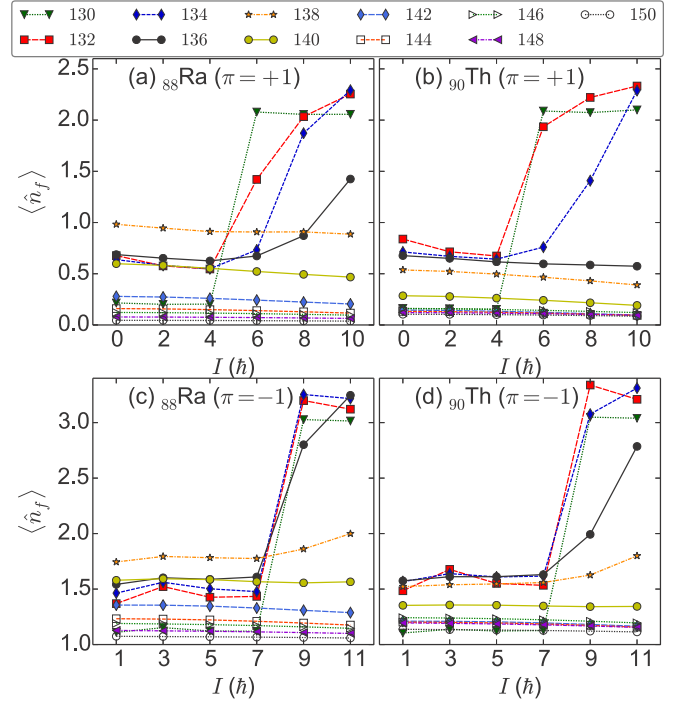


FIG. 5. The *f*-boson contents in the wave functions of the (a, b) even-spin positive-parity and (c, d) odd-spin negative-parity yrast states in $^{218-238}\text{Ra}$ and $^{220-240}\text{Th}$, obtained as the expectation value $\langle \hat{n}_f \rangle$ in a given state, are plotted as functions of the spin *I*. Different symbols denote the calculated quantities $\langle \hat{n}_f \rangle$ for the considered nuclei (their neutron numbers are indicated in the legend on the top) and are connected by lines.

role up to $N \approx 140$ even at low spins; i.e., the average value $\langle \hat{n}_f \rangle$ tends to be larger for lighter isotopes and becomes much smaller without significant changes for heavier isotopes. For the lighter isotopes the mixing of different configurations in the *sdf*-IBM states is pronounced.

B. Possible alternating-parity band structure

As a more quantitative measure of the extent to which the predicted positive- and negative-parity bands resemble alternating-parity bands, we have considered the quantity

$$S(I) = E(I+1) + E(I-1) - 2E(I), \quad (10)$$

where $E(I)$ represents the excitation energy of the $I = 0^+, 1^-, 2^+, \dots$ yrast states. In the limit of an ideal alternating-parity band, this quantity goes to zero. The quantity $S(I)$ is depicted in Fig. 6 as a function of the spin *I*. For most of the isotopes in both chains, the $S(I)$ values exhibit an odd-even staggering pattern. This staggering pattern is less pronounced for $N \approx 136$, reflecting that the negative-parity band becomes particularly low in energy and forms an approximate alternating-parity structure with the positive-parity ground-state band. For $N \geq 138$, the staggering is even more pronounced indicating that the positive- and negative-parity bands are decoupled from each other, a typical octupole vibrational feature associated with the β_3 softness of the potential.

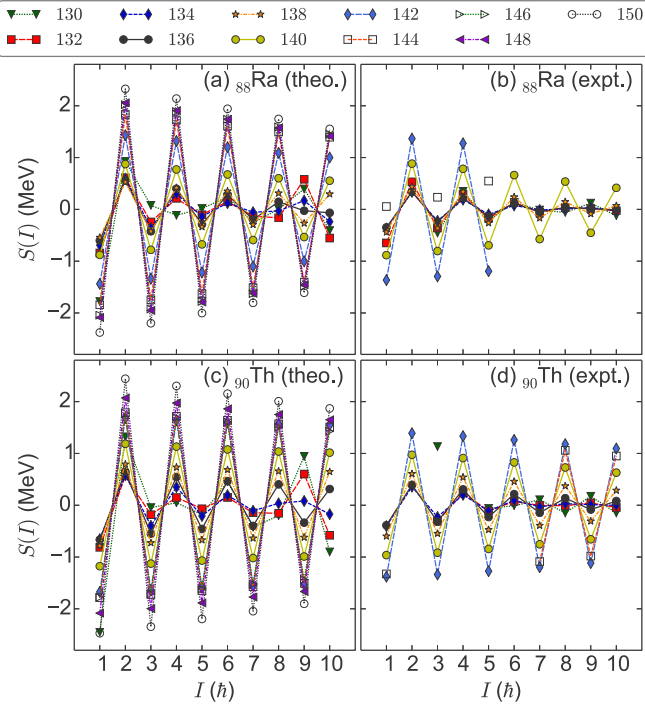


FIG. 6. The relative energy splitting between positive- and negative-parity yrast bands $S(I)$ [Eq. (10)], obtained for $^{218-238}\text{Ra}$ and $^{220-240}\text{Th}$, is plotted as a function of the spin I . The legend on the top indicates the neutron numbers for those nuclei that are plotted in each panel.

C. Transition strength properties

For the computation of the reduced transition probabilities, we employed the quadrupole and octupole transition operators:

$$\hat{T}^{E2} = e_B^{(2)} \hat{Q}_2, \quad \hat{T}^{E3} = e_B^{(3)} \hat{Q}_3, \quad (11)$$

where $e_B^{(\lambda)}$'s are effective charges and

$$\hat{Q}_2 = s^\dagger \tilde{d} + d^\dagger s + \chi'_{dd} [d^\dagger \times \tilde{d}]^{(2)} + \chi'_{ff} [f^\dagger \times \tilde{f}]^{(2)}, \quad (12)$$

$$\hat{Q}_3 = s^\dagger \tilde{f} + f^\dagger s + \chi'_{df} [d^\dagger \times \tilde{f} + f^\dagger \times \tilde{d}]^{(3)}. \quad (13)$$

The quadrupole and octupole transition operators in Eqs. (11) have the same form as the ones in the Hamiltonian equations (6)–(8) but with new parameters χ'_{dd} , χ'_{ff} , and χ'_{df} . The effective charges $e_B^{(\lambda)}$ are determined so that the intrinsic quadrupole (octupole) moment in the IBM, obtained as the expectation value of the operator $\hat{T}^{E\lambda}$ in the coherent state at the minimum of the PES [50], is equal to the Gogny-HFB one. Introducing the bosonic deformation parameters $\tilde{\beta}_\lambda = C_\lambda \beta_\lambda$, corresponding to the minimum of the PES, we obtain the following equations:

$$e_B^{(2)} \frac{N_B (2\tilde{\beta}_2 - \sqrt{\frac{2}{7}} \chi'_{dd} \tilde{\beta}_2^2 - \frac{2}{\sqrt{21}} \chi'_{ff} \tilde{\beta}_3^2)}{1 + \tilde{\beta}_2^2 + \tilde{\beta}_3^2} = Q_{20}^{\min} \quad (14)$$

$$e_B^{(3)} \frac{N_B \tilde{\beta}_3 (1 - \frac{2}{\sqrt{15}} \chi'_{df} \tilde{\beta}_2)}{1 + \tilde{\beta}_2^2 + \tilde{\beta}_3^2} = Q_{30}^{\min}. \quad (15)$$

For the parameter χ'_{dd} we have adopted the value $\chi'_{dd} = -\sqrt{7}/2$ obtained in the SU(3) limit [50]. However, we have taken the averages $\chi'_{ff} = 1.5$ and $\chi'_{df} = -1.6$ of the χ_{ff} and χ_{df} values employed for the Hamiltonian, respectively. The effective charges $e_B^{(2)}$ and $e_B^{(3)}$ have been further multiplied by the scale factors s_1 and s_2 , respectively. The scale factor s_1 is assumed to take the form $s_1 = 1.55/(9.3 - 0.3N_B)$, in order to reproduce the experimental systematic of the $B(E2; 2_1^+ \rightarrow 0_1^+)$ values. The boson-number dependence in the denominator of s_1 was introduced so that the computed $B(E2; 2_1^+ \rightarrow 0_1^+)$ is not too large for $N = 150$ isotopes (close to the neutron mid-shell $N = 154$). However, we considered $s_2 = 0.33$ so that an overall agreement with the systematics of the experimental $B(E3; 3_1^- \rightarrow 0_1^+)$ values is obtained.

The effective charges $e_B^{(2)}$ and $e_B^{(3)}$ (in $\sqrt{\text{W.u.}}$ units), Eqs. (14) and (15), are plotted in Figs. 3(k) and 3(l) as functions of the neutron boson number N_B . The effective charge $e_B^{(2)}$ increases smoothly with the neutron number while $e_B^{(3)}$ exhibits a parabolic behavior with a maximum at $N_B \approx 5$ that corresponds to neutron numbers $N \approx 136$ at which the most pronounced octupole deformations are found.

The electric dipole ($E1$) mode is yet another characteristic property of pear-shaped nuclei. In the *sdf*-IBM framework, the $E1$ operator reads

$$\hat{T}^{E1} = e_B^{(1)} (d^\dagger \times \tilde{f} + f^\dagger \times \tilde{d})^{(1)}, \quad (16)$$

with the $E1$ effective charge $e_B^{(1)}$. We have taken $e_B^{(1)} = 0.0277 e_B^{(1)}/b^{1/2}$ in order to reproduce the experimental $B(E1; 1_1^- \rightarrow 0_1^+)$ value for ^{222}Ra .

The predicted $B(E2; 2_1^+ \rightarrow 0_1^+)$, $B(E3; 3_1^- \rightarrow 0_1^+)$, and $B(E1; 1_1^- \rightarrow 0_1^+)$ transition rates are compared in Fig. 7 with the available experimental data. The increase in the $B(E2)$ values [Figs. 7(a) and 7(b)] correlates well with the increase in quadrupole collectivity along the studied isotopic chains. The $B(E3)$ strengths [Figs. 7(c) and 7(d)] display a parabolic behavior, similar to the one obtained for the excitation energies of negative-parity states, with a maximum around the neutron number $N = 136$.

The $B(E1; 1_1^- \rightarrow 0_1^+)$ strengths [Figs. 7(e) and 7(f)] increase smoothly. The predicted $B(E1)$ values reproduce reasonably well the experimental ones for $^{218-222}\text{Ra}$ and $^{220-226}\text{Th}$. However, the calculations are not able to account for the experimental $B(E1)$ values in ^{224}Ra and $^{228,230}\text{Th}$. Here, one should keep in mind that $E1$ transitions are less collective in nature and very sensitive to the occupancy of high- j orbitals around the Fermi surface [20,22]. Due to this sensitivity to single particle properties, specific details of $E1$ transitions may be, at least for some nuclear systems, out of reach for the IBM description (based on collective nucleon pairs) employed in this study. Phenomenological IBM studies (see, for example, Refs. [57,58,60,61]) have often considered the dipole $L = 1^-$ (p) boson to effectively describe $E1$ transitions. However, such a boson has not been included in this work since its microscopic origin is less clear than for the s , d , and f bosons.

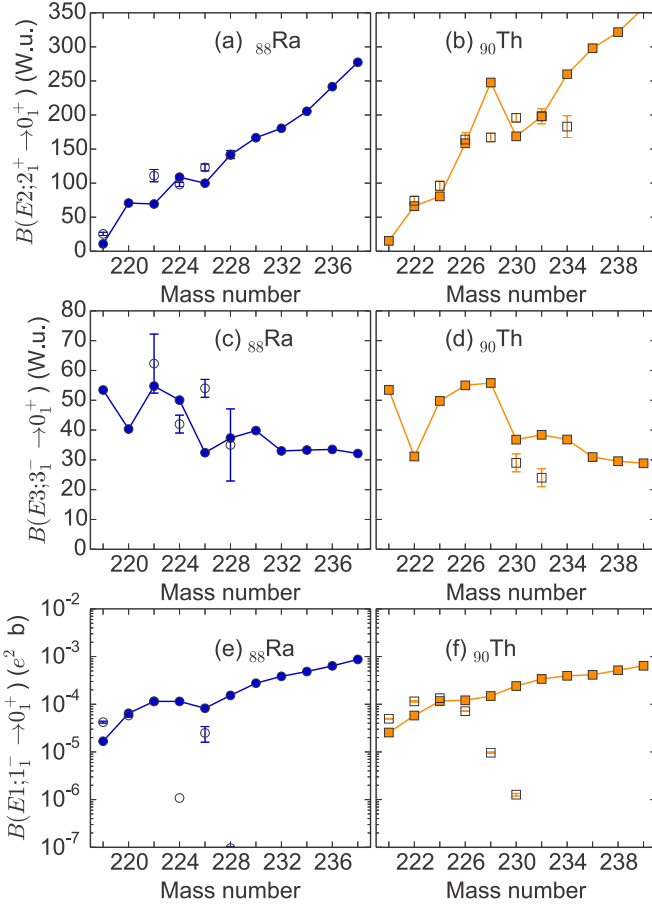


FIG. 7. Reduced transition probabilities (a, b) $B(E2; 2^+ \rightarrow 0^+)$, (c, d) $B(E3; 3^- \rightarrow 0^+)$, and (e, f) $B(E1; 1^- \rightarrow 0^+)$ for $^{218-238}\text{Ra}$ and $^{220-240}\text{Th}$. Theoretical values are represented by filled symbols connected by lines. Experimental values were taken from Refs. [5,6,59]. They are represented by open symbols with error bars. The $B(E2)$ and $B(E3)$ rates are in Weisskopf units while the $B(E1)$ rates in $e^2 b$ units are plotted using a logarithmic scale.

D. Transition quadrupole and octupole moments

The quadrupole $Q_2(I \rightarrow I - 2)$ as well as the octupole $Q_3(I \rightarrow I - 3)$ and $Q_3(I \rightarrow I - 1)$ moments, obtained from the reduced matrix elements $\langle I - 2 || \hat{T}^{E2} || I \rangle$, $\langle I - 3 || \hat{T}^{E3} || I \rangle$, and $\langle I - 1 || \hat{T}^{E3} || I \rangle$, are often considered signatures of quadrupole and octupole collectivity. Those transition multipole ($\lambda = 2, 3$) moments can be expressed as

$$\sqrt{2I+1} \sqrt{\frac{2\lambda+1}{16\pi}} (I\lambda 00 | I'0) Q_\lambda(I \rightarrow I') = \langle I' || \hat{T}^{E\lambda} || I \rangle, \quad (17)$$

where $(I\lambda 00 | I'0)$ denotes a Clebsch-Gordan coefficient. These quantities were computed for the in-band $E2$ transitions within $K^\pi = 0^+$ and $K^\pi = 0^-$ bands with $|I - I'| = \Delta I = 2$, and for the $\Delta I = 3$ and $\Delta I = 1$ $E3$ transitions between the $K^\pi = 0^+$ and $K^\pi = 0^-$ states. They were computed up to the spin $I^\pi = 8^+$.

The transition quadrupole and octupole moments, obtained for $^{218-238}\text{Ra}$ and $^{220-240}\text{Th}$, are shown in Fig. 8 as

functions of the spin I . The quadrupole moments [Figs. 8(a) and 8(b)] remain rather constant with spin although a certain staggering pattern is observed. In the case of the octupole moments, depicted in Figs. 8(c)–8(f), the lightest isotopes display rather irregular patterns with spin. However, the amplitudes of the oscillations become smaller for $130 \leq N \leq 136$, i.e., as one approaches stable octupole deformation. On average the computed Q_3 moments, for both the $\Delta I = 1$ and $\Delta I = 3$ transitions, are around $2000 e \text{ fm}^3$.

E. Low-energy excitation spectra, reduced transition probabilities, and reduced matrix elements for selected Ra isotopes

In what follows, the low-energy excitation spectra predicted for $^{224,226}\text{Ra}$ are discussed in detail to further examine the predicted power of the employed IBM framework based on the Gogny-D1M EDF. The energy spectrum obtained for ^{224}Ra is compared with the experimental one [5] in the top panel of Fig. 9. The ground-state $K^\pi = 0^+$ band is reproduced reasonably well by the calculations up to $I^\pi = 6^+$. However, for $I^\pi \geq 8^+$ the predicted band looks stretched as compared with the experiment. As can be seen from Fig. 5, in the case of ^{224}Ra , the f -boson content of states with $I^\pi \leq 8^+$ is $\langle \hat{n}_f \rangle \approx 0.7$ while for $I^\pi \geq 10^+$ the f -boson content turns out to be $\langle \hat{n}_f \rangle \approx 1.5$. For the $K^\pi = 0^-$ band, the 1^- (bandhead) state is higher in energy than the experimental one, although features such as the moment of inertia and energy spacing agree well with the experiment. Up to $I^\pi = 7^-$ the f -boson content of the band is $\langle \hat{n}_f \rangle \approx 1.4$ while for $I^\pi = 9^-$ more f bosons start to play a role, i.e., $\langle \hat{n}_f \rangle \approx 3.0$. Alternating-parity doublets are visible, in both the theoretical and experimental spectra, from $I^\pi = 5^-$. The predicted nonyrast 0_2^+ and 2_2^+ states (above 1 MeV) have also been included in the figure. These states have a double octupole phonon nature with $\langle \hat{n}_f \rangle \approx 2$. In the bottom panel of Fig. 9, we also plotted the energy spectrum obtained for ^{226}Ra . This spectrum compares slightly better with the experiment than in the case of ^{224}Ra . Here, the change in the structure of states in the $K^\pi = 0^+$ ($K^\pi = 0^-$) band is less pronounced with $\langle \hat{n}_f \rangle \approx 0.8-0.9$ ($\langle \hat{n}_f \rangle \approx 1.5-1.9$) up to $I^\pi = 16^+$ ($I^\pi = 11^-$). Similar results are found for $^{226,228}\text{Th}$.

The $B(E2)$ and $B(E3)$ transition rates obtained for ^{224}Ra are shown in Table I. We observe a very reasonable agreement with the corresponding experimental values. The only exceptions are the $B(E2; 5^- \rightarrow 3^-)$ and $B(E3; 1^- \rightarrow 2^+)$ transitions which are underestimated by a factor of 2 to 3. In addition, we also included in the table results from previous IBM calculations based on the relativistic DD-PC1 EDF [44]. As can be seen, both (mapped) IBM calculations provide rather similar predictions for the $B(E2)$ and $B(E3)$ rates. The $B(E1; 1^- \rightarrow 2^+)$ values obtained in the present study compare slightly better with the experiment. However, other $E1$ transition strengths are larger than the ones obtained in Ref. [44] typically by one order of magnitude and overestimate the experiment [5] by a factor from 10^2 to 10^3 .

Finally, let us have a look at the reduced matrix elements $|\langle I - 2 || \hat{T}^{E2} || I \rangle|$, $|\langle I - 3 || \hat{T}^{E3} || I \rangle|$, and $|\langle I - 1 || \hat{T}^{E3} || I \rangle|$ in the case of $^{222-228}\text{Ra}$ for which experimental data are available [5,6,62]. They are depicted in Fig. 10 as functions of I . The

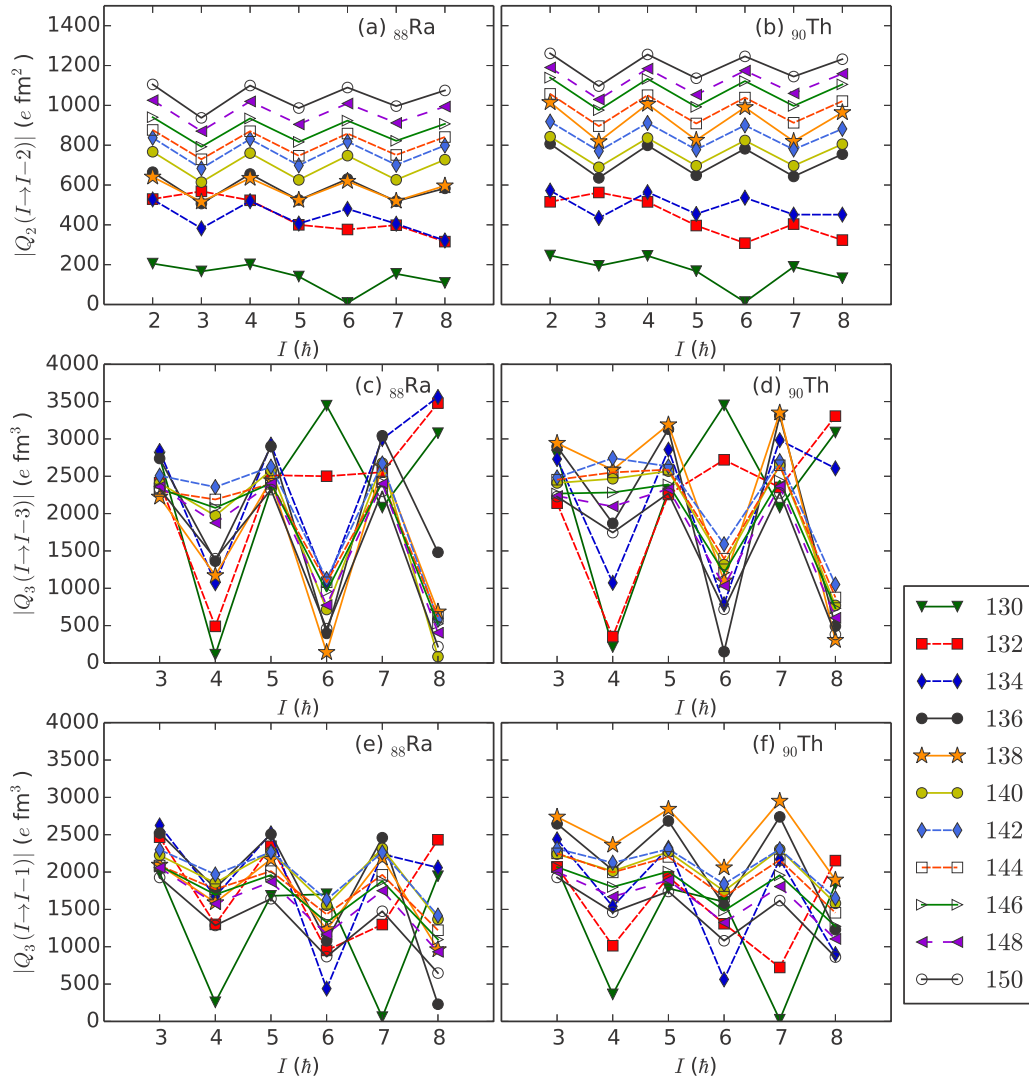


FIG. 8. The transition quadrupole and octupole moments (in $e \text{ fm}^\lambda$ units) obtained for $^{218-238}\text{Ra}$ and $^{220-240}\text{Th}$ are plotted as functions of the spin I . Different symbols represent the calculated quadrupole and octupole moments for the considered nuclei (their neutron numbers are indicated in the legend on the right) and are connected by lines. For more details, see the main text.

predicted $E2$ matrix elements [Figs. 10(a₁)–10(a₄)] increase with spin and agree reasonably well with the experimental ones. For some of the studied nuclei, the $E2$ matrix elements are almost zero at high spins (for example, at $I = 12^+$ for ^{224}Ra and at $I = 15^-$ for ^{226}Ra). This is probably due to band mixing effects occurring in the high-spin regime, as can be expected from the structural changes in the corresponding wave functions (see Fig. 5). The $|\langle I - 3 || \hat{T}^{E3} || I \rangle|$ [Figs. 10(b₁)–10(b₄)] and $|\langle I - 1 || \hat{T}^{E3} || I \rangle|$ [Figs. 10(c₁)–10(c₄)] matrix elements also increase as functions of I . However, they exhibit a pronounced staggering even at low spin that contradicts the pattern observed in the available experimental data. A similar staggering was also obtained in previous IBM studies [44,57]. It has been concluded, within the framework of the phenomenological *spdf* IBM model [57], that at least $3pf$ bosons ($n_p + n_f = 3$) are required to account for the experimental systematics of the reduced $E1$ matrix elements that linearly increase with spin. It would be interesting to examine whether the inclusion of the p -boson degree of freedom

can also improve the systematics of the $E3$ transitions in the (mapped) IBM framework. Another possible remedy for the staggering problem observed in the $E3$ and $E1$ transition matrix elements within the *sdf* IBM framework could be to consider higher-order terms in the corresponding transition operators [63] [see Eqs. (13) and (16)].

V. SUMMARY

In this paper, we considered the quadrupole-octupole coupling and collective excitations in the even-even actinides $^{218-238}\text{Ra}$ and $^{220-240}\text{Th}$ due to the renewed experimental interest in the region. The constrained Gogny-D1M HFB approach was employed to obtain (axially symmetric) quadrupole-octupole SCMF PESs. The SCMF PESs were mapped onto the corresponding IBM PESs using the expectation value of the *sdf* IBM Hamiltonian in the boson condensate state. The strength parameters of the bosonic Hamiltonian were determined via this mapping procedure. The wave functions

resulting from the diagonalization of the (mapped) *sdf* IBM Hamiltonian were used to compute octupole-related quantities such as, for example, both positive- and negative-parity excitation spectra and transition strengths.

The SCMF PESs are rather soft along the β_3 direction. A global mean-field reflection-asymmetric minimum emerges at $N = 132$ (i.e., for ^{220}Ra and ^{222}Th). For both isotopic chains, the most pronounced octupole deformation effects are found at $N = 136$ (i.e., for ^{224}Ra and ^{226}Th). This agrees well with the experimental findings of stable pearlike shapes for this particular neutron number. The octupole deformed minimum becomes less prominent with increasing neutron number and disappears from $N = 142$ (i.e., for ^{230}Ra and ^{232}Th) onward. These features are also found in the mapped *sdf* IBM PESs which nicely reproduce the basic topology of the fermionic PESs around the global minima.

The spectroscopic properties, resulting from the diagonalization of the *sdf* IBM Hamiltonian, were studied in detail. Within this context a parabolic behavior, centered around the nuclei ^{224}Ra and ^{226}Th , was found for the low-lying negative-parity spectra and the $B(E3; 3_1^- \rightarrow 0_1^+)$ reduced transition probabilities. For isotopes in the neighborhood of $N = 136$, an approximate alternating-parity band structure was found. Octupole-related properties were analyzed in detail for $^{222,224,226,228}\text{Ra}$. The calculations reproduce reasonably well the trends observed in the data available from Coulomb ex-

TABLE I. Theoretical and experimental $B(E2)$, $B(E3)$, and $B(E1)$ transition rates (in Weisskopf units) for ^{224}Ra . Experimental values are taken from Ref. [5]. For comparison, results based on the relativistic DD-PC1 EDF [44] are also included in the table. All transitions, with the exception of $B(E2; 2_2^+ \rightarrow 0^+)$, are between yrast states.

	Experiment	Theory	Ref. [44]
$B(E2; 2^+ \rightarrow 0^+)$	98 ± 3	109	109
$B(E2; 3^- \rightarrow 1^-)$	93 ± 9	81	71
$B(E2; 4^+ \rightarrow 2^+)$	137 ± 5	151	152
$B(E2; 5^- \rightarrow 3^-)$	190 ± 60	103	97
$B(E2; 6^+ \rightarrow 4^+)$	156 ± 12	154	159
$B(E2; 8^+ \rightarrow 6^+)$	180 ± 60	138	153
$B(E2; 2_2^+ \rightarrow 0^+)$	1.3 ± 0.5	4.9	0
$B(E3; 3^- \rightarrow 0^+)$	42 ± 3	50	42
$B(E3; 1^- \rightarrow 2^+)$	210 ± 40	86	85
$B(E3; 3^- \rightarrow 2^+)$	<600	57	46
$B(E3; 5^- \rightarrow 2^+)$	61 ± 17	85	61
$B(E1; 1^- \rightarrow 0^+)$	$<5 \times 10^{-5}$	4.8×10^{-3}	2.0×10^{-3}
$B(E1; 1^- \rightarrow 2^+)$	$<1.3 \times 10^{-4}$	5.9×10^{-4}	1.1×10^{-3}
$B(E1; 3^- \rightarrow 2^+)$	$3.9_{-1.4}^{+1.7} \times 10^{-5}$	1.4×10^{-2}	3.7×10^{-3}
$B(E1; 5^- \rightarrow 4^+)$	$4_{-2}^{+3} \times 10^{-5}$	2.4×10^{-2}	5.0×10^{-3}
$B(E1; 7^- \rightarrow 6^+)$	$<3 \times 10^{-4}$	3.5×10^{-2}	5.8×10^{-3}

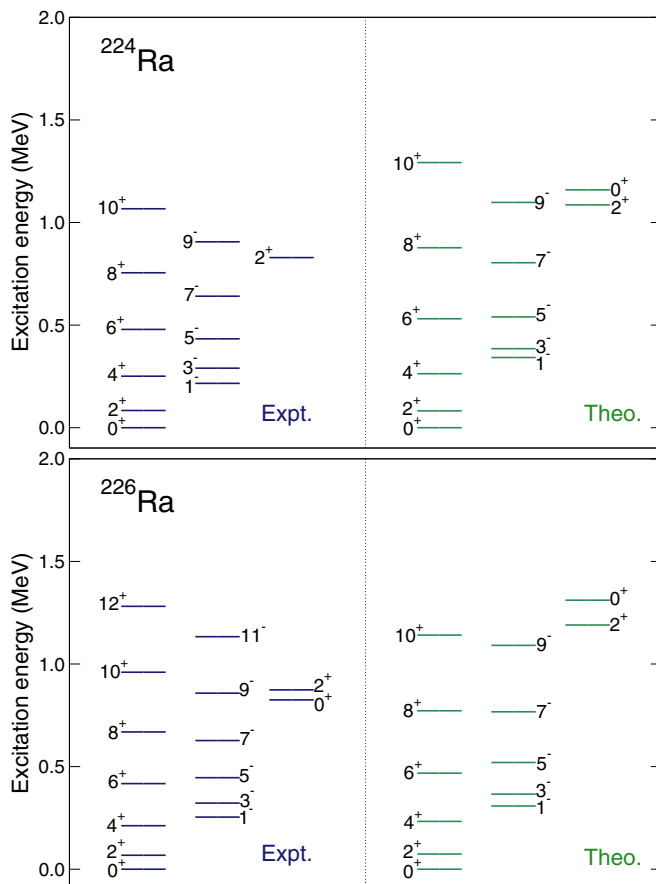


FIG. 9. The energy spectra obtained for ^{224}Ra (top) and ^{226}Ra (bottom) are compared with the experimental ones [5].

citation experiments. However, the fact that the calculations cannot account for the correct systematics of the $B(E1; 1_1^+ \rightarrow 0_1^+)$ rates and/or the $E3$ transition matrix elements suggests that improvements, such as the inclusion of dipole p bosons, are still required in the employed mapping procedure.

From the comparison of the results obtained in this work with the available experimental data as well as with previous (mapped) IBM calculations based on the relativistic mean-field approximation [43,44], we conclude that the trends predicted for the studied nuclei are independent of the underlying microscopic input; i.e., they are robust. Given the predictive power and computational advantages of the mapping procedure together with the IBM, studies of octupolarity in odd-mass actinides and heavier nuclear systems appear as our next plausible steps.

ACKNOWLEDGMENTS

This work has been supported by the Tenure Track Pilot Programme of the Croatian Science Foundation and the École Polytechnique Fédérale de Lausanne, and the Project TTP-2018-07-3554 Exotic Nuclear Structure and Dynamics, with funds of the Croatian-Swiss Research Programme. The work of L.M.R. was supported by Spanish Ministry of Economy and Competitiveness (MINECO) Grant No. PGC2018-094583-B-I00. This work has been partially supported by the Ministerio de Ciencia e Innovación (Spain) under Project No. PID2019-104002GB-C21, by the Consejería de Economía, Conocimiento, Empresas y Universidad de la Junta de Andalucía (Spain) under Group FQM-370, by the European Regional Development Fund (ERDF), No. SOMM17/6105/UGR, and by the European Commission, No. H2020-INFRAIA-2014-2015 (ENSAR2).

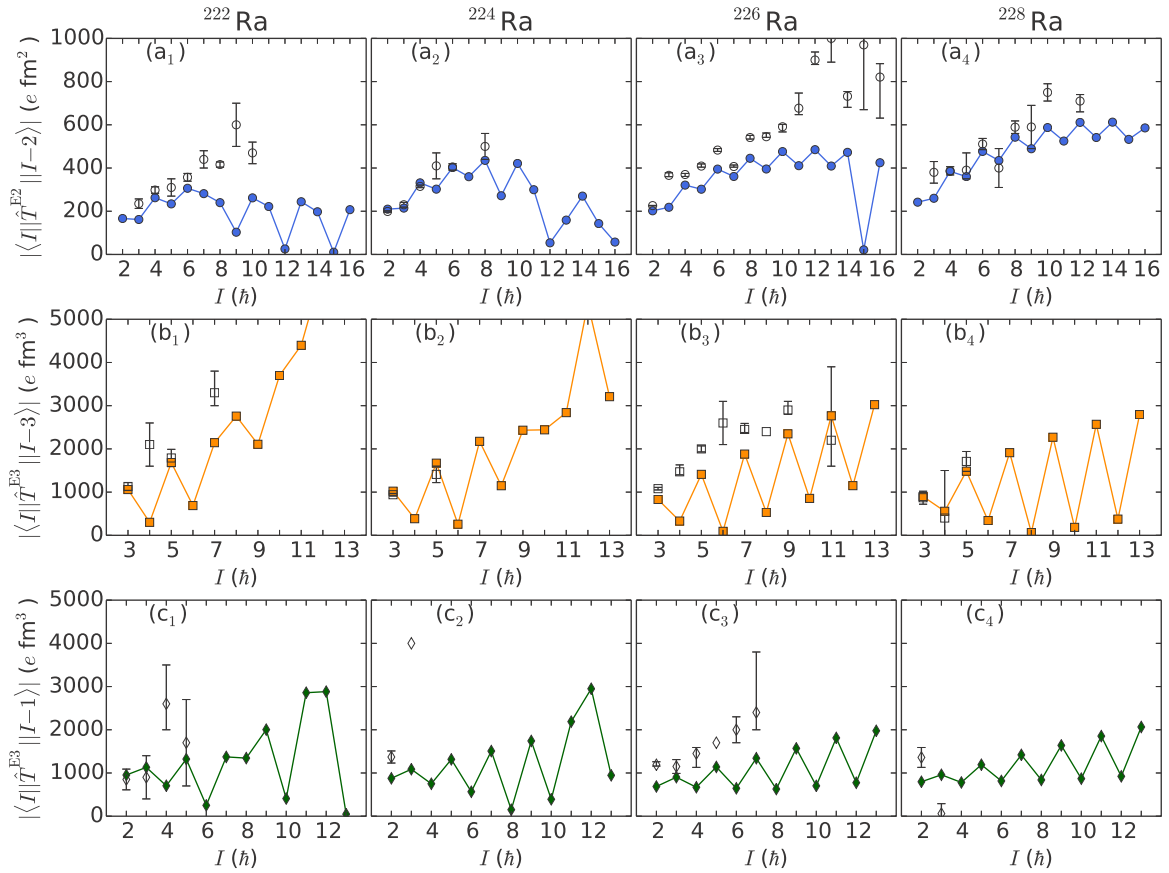


FIG. 10. Reduced matrix elements $|\langle I-2||\hat{T}^{E2}||I\rangle|$, $|\langle I-3||\hat{T}^{E3}||I\rangle|$, and $|\langle I-1||\hat{T}^{E3}||I\rangle|$ for $^{222,224,226,228}\text{Ra}$. Experimental data are taken from Refs. [6] ($^{222,228}\text{Ra}$), [5] (^{224}Ra), and [62] (^{226}Ra). Theoretical values are represented by filled symbols connected by lines. Experimental data are shown as open symbols with error bars. Experimental values without error bars represent upper limits [5,62].

Resources supporting this work were provided by the CEAFMC and the Universidad de Huelva High Performance

Computer (HPC@UHU) funded by ERDF/MINECO Project No. UNHU-15CE-2848.

- [1] P. A. Butler and W. Nazarewicz, *Rev. Mod. Phys.* **68**, 349 (1996).
- [2] P. A. Butler, *J. Phys. G: Nucl. Part. Phys.* **43**, 073002 (2016).
- [3] L. M. Robledo and G. F. Bertsch, *Phys. Rev. C* **84**, 054302 (2011).
- [4] L. M. Robledo, *J. Phys. G: Nucl. Part. Phys.* **42**, 055109 (2015).
- [5] L. P. Gaffney, P. A. Butler, M. Scheck, A. B. Hayes, F. Wenander, M. Albers, B. Bastin, C. Bauer, A. Blazhev, S. Bönig *et al.*, *Nature (London)* **497**, 199 (2013).
- [6] P. A. Butler, L. P. Gaffney, P. Spagnoletti, K. Abrahams, M. Bowry, J. Cederkäll, G. de Angelis, H. De Witte, P. E. Garrett, A. Goldkuhle *et al.*, *Phys. Rev. Lett.* **124**, 042503 (2020).
- [7] B. Bucher, S. Zhu, C. Y. Wu, R. V. F. Janssens, D. Cline, A. B. Hayes, M. Albers, A. D. Ayangeakaa, P. A. Butler, C. M. Campbell *et al.*, *Phys. Rev. Lett.* **116**, 112503 (2016).
- [8] B. Bucher, S. Zhu, C. Y. Wu, R. V. F. Janssens, R. N. Bernard, L. M. Robledo, T. R. Rodríguez, D. Cline, A. B. Hayes, A. D. Ayangeakaa *et al.*, *Phys. Rev. Lett.* **118**, 152504 (2017).
- [9] J. Engel, M. J. Ramsey-Musolf, and U. van Kolck, *Prog. Part. Nucl. Phys.* **71**, 21 (2013).
- [10] D. Vretenar, A. Afanasjev, G. Lalazissis, and P. Ring, *Phys. Rep.* **409**, 101 (2005).
- [11] T. Nikšić, D. Vretenar, and P. Ring, *Prog. Part. Nucl. Phys.* **66**, 519 (2011).
- [12] M. Bender, P.-H. Heenen, and P.-G. Reinhard, *Rev. Mod. Phys.* **75**, 121 (2003).
- [13] L. M. Robledo, T. R. Rodríguez, and R. R. Rodríguez-Guzmán, *J. Phys. G: Nucl. Part. Phys.* **46**, 013001 (2019).
- [14] S. Marcos, H. Flocard, and P. Heenen, *Nucl. Phys. A* **410**, 125 (1983).
- [15] P. Bonche, P. Heenen, H. Flocard, and D. Vautherin, *Phys. Lett. B* **175**, 387 (1986).
- [16] P. Bonche, S. J. Krieger, M. S. Weiss, J. Dobaczewski, H. Flocard, and P.-H. Heenen, *Phys. Rev. Lett.* **66**, 876 (1991).
- [17] P.-H. Heenen, J. Skalski, P. Bonche, and H. Flocard, *Phys. Rev. C* **50**, 802 (1994).
- [18] L. Robledo, J. Egido, J. Berger, and M. Girod, *Phys. Lett. B* **187**, 223 (1987).
- [19] L. Robledo, J. Egido, B. Nerlo-Pomorska, and K. Pomorski, *Phys. Lett. B* **201**, 409 (1988).
- [20] J. Egido and L. Robledo, *Nucl. Phys. A* **518**, 475 (1990).

- [21] J. Egido and L. Robledo, *Nucl. Phys. A* **524**, 65 (1991).
- [22] J. Egido and L. Robledo, *Nucl. Phys. A* **545**, 589 (1992).
- [23] E. Garrote, J. L. Egido, and L. M. Robledo, *Phys. Rev. Lett.* **80**, 4398 (1998).
- [24] E. Garrote, J. Egido, and L. Robledo, *Nucl. Phys. A* **654**, 723c (1999).
- [25] W. Long, J. Meng, N. Van Giai, and S.-G. Zhou, *Phys. Rev. C* **69**, 034319 (2004).
- [26] L. M. Robledo, M. Baldo, P. Schuck, and X. Viñas, *Phys. Rev. C* **81**, 034315 (2010).
- [27] J. Erler, K. Langanke, H. P. Loens, G. Martínez-Pinedo, and P.-G. Reinhard, *Phys. Rev. C* **85**, 025802 (2012).
- [28] L. M. Robledo and R. R. Rodríguez-Guzmán, *J. Phys. G: Nucl. Part. Phys.* **39**, 105103 (2012).
- [29] R. Rodríguez-Guzmán, L. M. Robledo, and P. Sarriguren, *Phys. Rev. C* **86**, 034336 (2012).
- [30] L. M. Robledo and P. A. Butler, *Phys. Rev. C* **88**, 051302(R) (2013).
- [31] R. N. Bernard, L. M. Robledo, and T. R. Rodríguez, *Phys. Rev. C* **93**, 061302(R) (2016).
- [32] S. E. Agbemava, A. V. Afanasjev, and P. Ring, *Phys. Rev. C* **93**, 044304 (2016).
- [33] S. E. Agbemava and A. V. Afanasjev, *Phys. Rev. C* **96**, 024301 (2017).
- [34] Z. Xu and Z.-P. Li, *Chin. Phys. C* **41**, 124107 (2017).
- [35] S. Y. Xia, H. Tao, Y. Lu, Z. P. Li, T. Nikšić, and D. Vretenar, *Phys. Rev. C* **96**, 054303 (2017).
- [36] S. Ebata and T. Nakatsukasa, *Phys. Scr.* **92**, 064005 (2017).
- [37] R. Rodríguez-Guzmán, Y. M. Humadi, and L. M. Robledo, *Eur. Phys. J. A* **56**, 43 (2020).
- [38] Y. Cao, S. E. Agbemava, A. V. Afanasjev, W. Nazarewicz, and E. Olsen, *Phys. Rev. C* **102**, 024311 (2020).
- [39] R. Rodríguez-Guzmán, Y. M. Humadi, and L. M. Robledo, *J. Phys. G: Nucl. Part. Phys.* **48**, 015103 (2021).
- [40] P. Ring and P. Schuck, *The Nuclear Many-Body Problem* (Springer-Verlag, Berlin, 1980).
- [41] K. Nomura, N. Shimizu, and T. Otsuka, *Phys. Rev. Lett.* **101**, 142501 (2008).
- [42] K. Nomura, N. Shimizu, and T. Otsuka, *Phys. Rev. C* **81**, 044307 (2010).
- [43] K. Nomura, D. Vretenar, and B.-N. Lu, *Phys. Rev. C* **88**, 021303(R) (2013).
- [44] K. Nomura, D. Vretenar, T. Nikšić, and B.-N. Lu, *Phys. Rev. C* **89**, 024312 (2014).
- [45] K. Nomura, R. Rodríguez-Guzmán, and L. M. Robledo, *Phys. Rev. C* **92**, 014312 (2015).
- [46] K. Nomura, T. Nikšić, and D. Vretenar, *Phys. Rev. C* **97**, 024317 (2018).
- [47] T. Nikšić, D. Vretenar, and P. Ring, *Phys. Rev. C* **78**, 034318 (2008).
- [48] J. Decharge, M. Girod, and D. Gogny, *Phys. Lett. B* **55**, 361 (1975).
- [49] S. Goriely, S. Hilaire, M. Girod, and S. Péru, *Phys. Rev. Lett.* **102**, 242501 (2009).
- [50] F. Iachello and A. Arima, *The Interacting Boson Model* (Cambridge University Press, Cambridge, UK, 1987).
- [51] J. Engel and F. Iachello, *Nucl. Phys. A* **472**, 61 (1987).
- [52] J. F. Berger, M. Girod, and D. Gogny, *Nucl. Phys. A* **428**, 23 (1984).
- [53] T. Otsuka, A. Arima, and F. Iachello, *Nucl. Phys. A* **309**, 1 (1978).
- [54] J. N. Ginocchio and M. W. Kirson, *Nucl. Phys. A* **350**, 31 (1980).
- [55] K. Nomura, T. Otsuka, N. Shimizu, and L. Guo, *Phys. Rev. C* **83**, 041302(R) (2011).
- [56] D. J. Thouless and J. G. Valatin, *Nucl. Phys.* **31**, 211 (1962).
- [57] N. V. Zamfir and D. Kusnezov, *Phys. Rev. C* **63**, 054306 (2001).
- [58] N. V. Zamfir and D. Kusnezov, *Phys. Rev. C* **67**, 014305 (2003).
- [59] Brookhaven National Nuclear Data Center, <http://www.nndc.bnl.gov>.
- [60] D. Kusnezov and F. Iachello, *Phys. Lett. B* **209**, 420 (1988).
- [61] M. Spieker, S. Pascu, A. Zilges, and F. Iachello, *Phys. Rev. Lett.* **114**, 192504 (2015).
- [62] H. J. Wollersheim, H. Emling, H. Grein, R. Kulesa, R. S. Simon, C. Fleischmann, J. de Boer, E. Hauber, C. Lauterbach, C. Schandera *et al.*, *Nucl. Phys. A* **556**, 261 (1993).
- [63] A. F. Barfield, P. von Brentano, A. Dewald, K. O. Zell, N. V. Zamfir, D. Bucurescu, M. Ivaşcu, and O. Scholten, *Z. Phys. A* **332**, 29 (1989).